PHYSICAL REVIEW B **87**, 064105 (2013)

Complex crystallization dynamics in amorphous germanium observed with dynamic transmission electron microscopy

Liliya Nikolova,[1] Thomas LaGrange,[2,*] Mark J. Stern,[3] Jennifer M. MacLeod,[1] Bryan W. Reed,[2] Heide Ibrahim,[1] Geoffrey H. Campbell,[2] Federico Rosei,[1,4,†] and Bradley J. Siwick[3,‡]

[1]*Institut National de la Recherche Scientifique, Centre Énergie, Matériaux, Télécommunications, 1650 Lionel Boulet Boulevard, Varennes, Quebec J3X 1S2, Canada*

[2]*Condensed Matter and Materials Division, Physical and Life Sciences Directorate, Lawrence Livermore National Laboratory, P.O. Box 808, Livermore, California 94551-0808, USA*

[3]*Departments of Physics and Chemistry, Center for the Physics of Materials, McGill University, 801 Sherbrooke St. W., Montreal, Quebec H3A 2K6, Canada*

[4]*Centre for Self-Assembled Chemical Structures, McGill University, 801 Sherbrooke St. W., Montreal, Quebec H3A 2K6, Canada*

(Received 15 October 2012; published 14 February 2013)

Crystallization of amorphous germanium (a-Ge) by laser or electron beam heating is a remarkably complex process that involves several distinct modes of crystal growth and the development of intricate microstructural patterns on the nanosecond to ten microsecond time scales. Here we use dynamic transmission electron microscopy (DTEM) to study the fast, complex crystallization dynamics with 10 nm spatial and 15 ns temporal resolution. We have obtained time-resolved real-space images of nanosecond laser-induced crystallization in a-Ge with unprecedentedly high spatial resolution. Direct visualization of the crystallization front allows for time-resolved snapshots of the initiation and roughening of the dendrites on submicrosecond time scales. This growth is followed by a rapid transition to a ledgelike growth mechanism that produces a layered microstructure on a time scale of several microseconds. This study provides insights into the mechanisms governing this complex crystallization process and is a dramatic demonstration of the power of DTEM for studying time-dependent material processes far from equilibrium.

DOI: 10.1103/PhysRevB.87.064105 PACS number(s): 64.70.kg, 81.10.−h, 68.37.Lp, 81.05.Gc

I. INTRODUCTION

Amorphous semiconductors are metastable and will spontaneously undergo a transition to the lower free energy crystalline state over a range of temperatures below the crystalline melting temperature (T_{mc}). This fact has been exploited for the fabrication of solar cells, flat panel displays, and IR detectors where thin amorphous films are rapidly crystallized by appropriate laser or electron beam heating. As previous work has shown,[1–13] the resulting crystalline microstructure can be extremely complex and depends on the details of the crystallization mechanism, the heating geometry, and a variety of possible morphological instabilities through a subtle interplay of kinetics and thermodynamics.

In all cases an essential feature of the crystallization is the latent heat released at the crystallization front, which is significant; the latent heat L for the amorphous-crystalline (a-c) transformation divided by the specific heat capacity c is $L/c \sim 450$ K in Ge.[10] Over certain substrate temperature ranges this release of energy can be sufficient to fuel a self-sustained crystallization front that propagates for distances as large as several centimeters. Since the process is accompanied by release of heat, sound, and light emission it has been termed explosive crystallization,[12] a phenomenon common to amorphous semiconductors and some metals.

Previous work has described two broad classes of explosive crystallization,[6,11] those in which the crystallization front involves a direct c-a interface [explosive solid phase crystallization (ESPC)] and those in which the a-c transformation is mediated by a metastable liquid layer [explosive liquid phase crystallization (ELPC)]. ELPC involves the copropagation of two interfaces, a crystal-liquid (c-l) interface at which crystallization occurs and a liquid-amorphous (l-a) interface some distance ahead of this crystallization front. The width of the liquid layer during ELPC in Si has been estimated experimentally by several techniques to be on the order 10 nm,[4,14,15] which is also broadly in agreement with the results of molecular dynamics (MD) simulations.[16]

The ELPC mechanism relies on the apparent difference in the melting temperatures (and enthalpies) between the amorphous and crystalline phases. Calorimetric studies have suggested that the amorphous phase undergoes a first-order phase transformation equivalent to melting at $T_{ma} \sim 0.8\ T_{mc} = 969$ K,[17] although the precise value depends on the state of relaxation of the amorphous film. Such a first-order transition has been observed in MD simulations of amorphous germanium using classical Stillinger-Weber-type interatomic potentials,[18] and indirectly in experiment through transient conductance and time-resolved reflectivity measurements in Si[15] and the redistribution of dopant impurities in Ge.[8] Equilibrium phase diagrams make it clear that this liquid is metastable in the temperature range $T_{ma} < T < T_{mc}$,[17] so the presence of a liquidlike phase as a transient intermediate along the crystallization pathway is due to kinetic factors; i.e., the rate of the a-l transition is fast compared to the direct a-c transformation over the same range of temperatures. This distinct kinetic pathway plays an important role in the resultant microstructure.

In this article our focus is on explosive crystallization dynamics in nanosecond laser-heated thin amorphous germanium films. The recent developments in dynamic transmission electron microscopy (DTEM) at LLNL[19–22] have provided an experimental platform capable of following the nanometer

scale evolution of the microstructure associated with this process *in situ* from its earliest stages (∼10 ns) to completion (∼10 μs) in unprecedented detail. We are able to follow the crystallization front as it evolves through three morphologically distinct crystalline zones, revealing important details of the crystallization dynamics at each stage. In particular, due to the unique nature of the DTEM observations,[20,23–25] we are able to address several important outstanding issues including the mechanisms for growth in the different regions and, in particular, how the rapid microstructural evolution and morphological changes during crystallization relate to an evolving temperature profile.

II. EXPERIMENTAL

Amorphous germanium films with a thickness of 110 nm were prepared by electron beam evaporation onto commercially available 40-nm thick silicon monoxide (SiO) membranes supported by 300-mesh copper grid (Ted Pella, Inc., Redding, California). The substrates were held at room temperature during the deposition process. The amorphous structure of these films was confirmed by glancing angle x-ray diffraction.

In situ time-resolved imaging was performed with the recently developed DTEM at Lawrence Livermore National Laboratory. This instrument permits *in situ* observation of laser-induced structural transformations with ∼10 nm spatial resolution and 15 ns temporal resolution and is described in detail in Refs. 20 and 22. The crystallization process is observed by performing multiple experiments on fresh areas with different time delays set between the cathode and drive lasers. The temporal uncertainty between measurements taken at different time delays is defined by the timing jitter between the two laser systems, ±1 ns. The incident laser fluence on the sample was kept constant at 110 mJ cm^{-2} ± 3% (532 nm, pulse duration 15 ns), which provides a heating rate of ∼7 × 10^{10} K/s[30] and initial temperature (before crystallization) of ∼1100 K towards the center of the illuminated region.

The time-dependent radial temperature profile was calculated using a two-dimensional (2D) finite element method implemented in MATLAB. This model includes the thermal diffusion of the initial laser deposited energy and the heat evolved at the crystallization front through a phenomenological source term. This source term is a cylindrically symmetric ring of crystallization whose position propagates outward (radially) at the experimentally determined front velocity, heating at a rate appropriate for the experimentally determined heat of crystallization, $L = 800$ J cm^{-3},[26] specific heat capacity, $C_p = 1.6$ J cm^{-3} K^{-1},[27] density, $\rho = 5.0 \pm 0.3$ g cm^{-3},[28] and thermal conductivity of a-Ge, $\kappa = 0.13$ W cm^{-1} K^{-1}.[29] This model was developed to explore the coarse behavior of the average temperature with time and radius through Zone II and Zone III (defined below) pertinent to the discussion and focus of this paper, not the detailed fine variations on the length scale of nanocrystallization.

III. RESULTS

In this section we present observations of the microstructural evolution in SiO supported a-Ge films following exposure to a single nanosecond laser pulse. The equilibrium post-mortem structure (i.e., when crystallization ceases) exhibits three distinct morphological regions, denoted Zones I–III, as shown in Fig. 1. This intricate rosette microstructure is a robust feature of both laser-induced[3] and electron-beam-induced[10] crystallization of a-Ge films and has been observed in previous studies. The aim of our study was to unravel the microstructural evolution in a-Ge films that leads to this complex crystallization pattern through direct observations of the crystallization front using the DTEM.

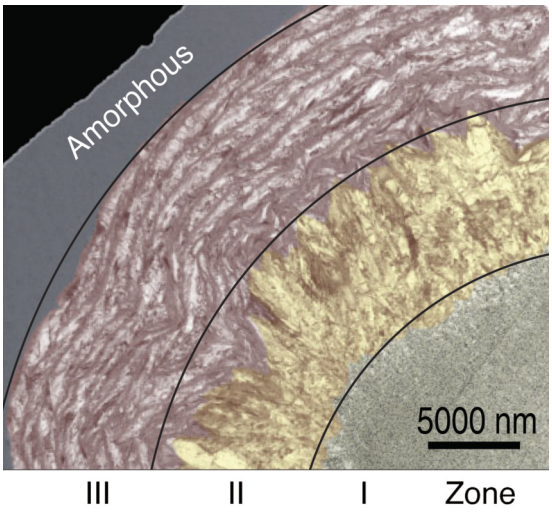

FIG. 1. (Color online) Complex laser-induced crystallization of a-Ge. Exposure of a thin (110 nm) a-Ge film to a single 15 ns laser pulse of sufficient fluence leads to crystallization in three morphologically distinct zones (I–III) as shown here. Only one quarter of the approximately cylindrically symmetric microstructure is shown. The radius of the Zone I boundary (indicated in the figure) is approximately equal to the $1/e^2$ radius diameter of the Gaussian laser spot profile exposing the specimen (45 μm in these experiments). False color was added to accentuate zone boundaries.

A. Zone I

The final microstructure exhibits a central nanocrystalline zone with a radius that is approximately equal to the $1/e^2$ radius of the Gaussian laser beam spot that initiates the crystallization (Fig. 1); $r \sim 45$ μm in this study. Nanocrystals in this region are randomly oriented and typically range in size from 10 nm to 100 nm with some crystallites as large as 300 nm.

A detailed study of the nucleation and growth kinetics in this nanocrystalline region was the subject of a previous publication,[30] and for completeness we summarize the results here. Near the center of this region where the film temperature reaches ∼1100 K (above the reported melting temperature for a-Ge, but below the melting temperature for crystalline germanium), DTEM observations show that supercritical nuclei are formed less than 20 ns after laser excitation and that complete crystallization of this local region occurs within ∼55 ns. From the count of the number of crystals in each time-resolved image the maximum nucleation rate was estimated to be ∼1.6 × 10^{22} nuclei cm^{-3} s^{-1}. The time for nanocrystallization increases away from the center of the laser

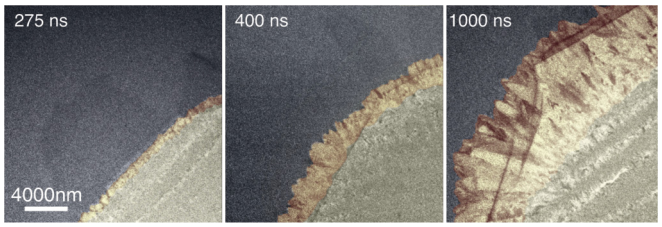

FIG. 2. (Color online) DTEM images of the time-evolving microstructure though Zone II. Large, radially elongated crystals nucleate at the Zone I boundary and grow outwards with a radial velocity of approximately 8 m/s. The initially flat explosive crystallization front (275 ns) develops microscopically smooth protrusions (400 ns) that show an increasingly faceted appearance toward the boundary with Zone III (1000 ns). False color was added to accentuate zone boundaries.

excitation spot, with Zone I crystallization completing ∼275 ns after laser excitation.

As described in the introduction, previous work suggests that under the excitation conditions used a-Ge melts to form a metastable liquid (i.e., a strongly supercooled liquid) prior to crystallization in Zone I. However, it is not possible to *a priori* define a DTEM image contrast level to distinguish between solid amorphous germanium and metastable liquid germanium at the same temperature. Therefore the state of the material in Zone I after photoexcitation and before crystallization is still an open question.

B. Zone II

Following the completion of the nanocrystalline Zone I, growth of large radially elongated crystals (LREC) is initiated. The lengths of the LREC forming Zone II are typically 6–10 μm and DTEM observations reveal that the growth of these crystals takes ∼1000 ns (starting ∼275 ns and ending ∼1300 ns after the laser excitation). Thus, the average growth velocity of the LREC in Zone II is 8 ± 2 m/s. The time-dependent crystallization front can be observed directly with DTEM (Fig. 2) and is seen to be relatively flat (Fig. 2, 275 ns) during the early stage of crystallization in Zone II, but the crystallization front rapidly develops protrusions. Initially smooth (Fig. 2, 400 ns), these protrusions evolve into a highly faceted interface (Fig. 2, 1000 ns) at the outer boundary of Zone II.

C. Zone III

A remarkable feature of the crystallization dynamics is the observation of an abrupt transition from the microstructure of Zone II (radially oriented dendrites) to a layered microstructure in Zone III (Fig. 1). These layers initially have a long axis following the boundary between Zones II and III, but become annularly/azimuthally arranged over a distance approximately equal to the roughness of the interface between these two zones. This banded microstructure is composed of layers of large elongated crystals (visible as white bands in Fig. 1) and nanocrystalline layers (visible as narrow dark bands in Fig. 1) that have a "feathered" morphology decorating the larger azimuthally tilted grains.

The banded microstructure of Zone III develops after completion of the LREC growth (∼1300 ns) and continues out to approximately 10 microseconds. DTEM observations of the crystallization front outside of the boundary region reveal that the growth direction for the large crystal layers is perpendicular to the direction of macroscopic crystallization (or to the net heat flow). This is indicated in Fig. 3(a), where a DTEM image at 7500 ns delay is shown. To clarify the relationship between the evolving microstructure at 7500 ns and that at the completion of crystallization [Fig. 3(b)], a complementary colorized image is shown in Fig. 3(c). Features in the final microstructure that are present at 7500 ns display as white in this image and those that are absent are colored pink. It is clear from the DTEM observations that crystallization in this region occurs through the formation of multiple azimuthally tilted crystals each with a local growth velocity in

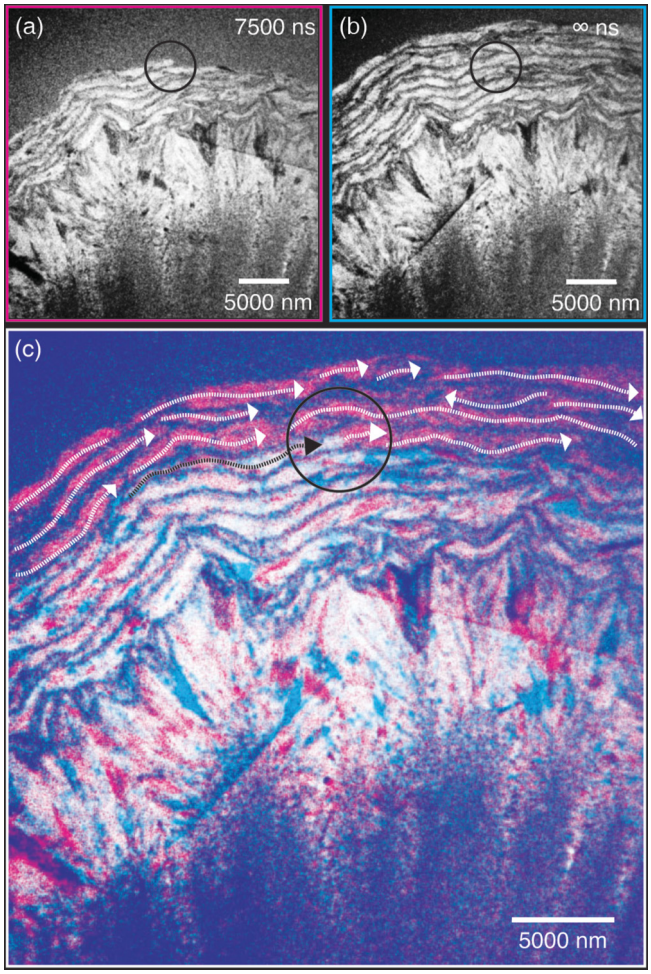

FIG. 3. (Color online) Explosive crystallization front in Zone III. (a) A DTEM image of the instantaneous microstructure 7500 ns after laser exposure. A partially formed outer layer is indicated with a circle. (b) The final microstructure at the completion of crystallization. (c) Stacked and colorized images showing the relationship between the instantaneous (white) and final (pink) microstructures. Growth in a single layer proceeds in the azimuthal direction at velocities similar to those observed in Zone II. The radial advance of crystallization occurs through the accumulation of additional layers as indicated schematically with dashed arrows.

the azimuthal direction [indicated schematically with arrows in Fig. 3(c)]. The progress of crystallization in the radial direction simply results from the accumulation of additional interleaved layers. Comparison of many time-resolved images accumulated over many specimen positions in this range of delays was used to estimate the Zone III radial growth velocity to be ~1 m/s, approximately an order of magnitude slower than that observed in Zone II. Single-layer growth velocities in the azimuthal direction, however, are likely much higher and comparable to the LREC growth rates (8 m/s) in Zone II.

IV. DISCUSSION

We will focus our discussion on the crystallization dynamics involved in the complex pattern formation in Zones II and III. As shown above, DTEM images have revealed that these zones are formed following a rapid burst of nucleation-controlled crystallization that leaves the film fine-grained and polycrystalline inside the $1/e^2$ diameter of the laser spot (within approximately 275 ns). Based on the thermal diffusivity of a-Ge ($D = 0.1$ cm^2/s),[10] the lateral thermal diffusion length in the a-Ge film over this brief time scale is $L_d = (4Dt)^{1/2} \sim 3$ μm. Thus, it is evident that the redistribution of thermal energy from the central polycrystalline region to the surrounding region (i.e., the area that will become Zone II and Zone III) is minimal before crystallization in Zone II begins. Crystallization in Zone II is initiated on a temperature profile only slightly perturbed from the initial, circularly symmetric Gaussian temperature field produced through laser excitation of the a-Ge material.

The morphology and growth dynamics of the large radially elongated crystals formed within Zone II suggest a change in the crystallization mode from nucleation dominated to growth controlled. The grains formed at the outer edge of Zone I act as the nuclei from which these LRECs grow. Once initiated, this growth mode is self-sustaining over a distance of ~10 μm due to the exothermic character of the crystallization and the underlying Gaussian temperature profile created through laser excitation.

A feature of the Zone II crystallization that has been revealed through these time-resolved images is the development of protrusions on the initially flat crystallization front (Fig. 2). Earlier work has suggested that the growth front of the LREC should remain smooth under the conditions of our experiment due to the Gibbs-Thomson effect.[3] We find that this effect is insufficient to maintain a flat interface in Zone II. Instead, the increasing amplitude of these protrusions is indicative of a Mullins-Sekerka-type instability[31,32] influencing the roughness of the advancing interface and giving rise to the dendritic morphology in Zone II. The instability is initiated by growth anisotropies, which perturb the local temperature profile. Once started, the instability grows due to the higher rate of heat dissipation at the tip of the protrusion roughening the planar crystallization front and producing the observed LREC. Using a simplified model that relates the growth rate of the dendrite (v) to its radius (r), thermal conductivity (κ_a), latent heat of crystallization (L_c), and temperature difference ($T_i - T_\infty$) between the interface (T_i) and surrounding material held at room temperature (T_∞), we can garner a qualitative interpretation of the growth mechanism as[33]

$$v = \frac{\kappa_a}{L_c r}(T_i - T_\infty). \quad (1)$$

The interfacial temperature necessary for the front to propagate at the observed 8 m/s for LREC having ~1.7 μm radii (Fig. 2) is calculated to be 1130 K using Eq. (1) and the material parameters provided in the Experimental section. This temperature exceeds the melting temperature of the a-Ge (969 K)[17] but is below the crystalline melt temperature (1210 K).[34] The observed dendritic instability and the growth rate model both strongly suggest that the crystallization front through Zone II is not a direct c-a interface, but rather crystallization proceeds via an ELPC mechanism with copropagating c-l and l-a interfaces.

An important question to be addressed is the change in crystallization dynamics at the outer edge of Zone II, where an abrupt change in crystallization behavior is evident. To address this point we have complemented the DTEM images (Figs. 2 and 3) with computations of the time-evolving average radial temperature profile [i.e., $T(r)$] in the film. This was accomplished by modeling the 2D heat flow problem in the film including the heat evolved at the crystallization front. These calculations show that, in the geometry of our experiment, the average temperature at the crystallization front drops through Zone II (Fig. 4), approximately following the decline of the underlying Gaussian temperature profile over the same distance. This provides an explanation for the increased faceting, i.e., the observation in the time-resolved images that initially rounded/smooth protrusions become increasingly faceted as growth becomes more anisotropic through Zone II (see Fig. 2). In addition, these calculations suggest that the

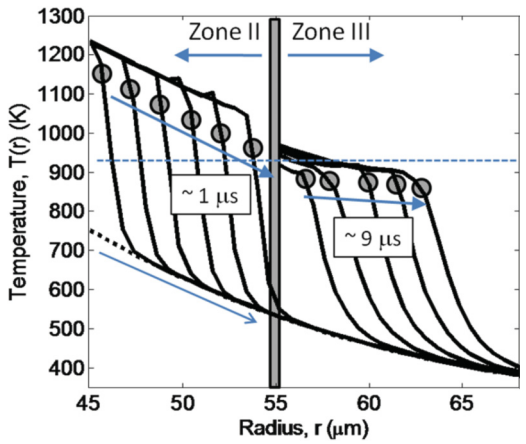

FIG. 4. (Color online) The time-evolving temperature profile in the crystallizing film. The computed coarse-grained, circularly symmetric radial temperature distribution in the film, $T(r)$, is shown in the vicinity of crystallization front for 150 ns time-steps through Zone II and 1.8 μs time-steps through Zone III. The radial position of the crystallization front at each time is indicated with a grey circle. The temperature decrease through Zone II approximately follows the decrease in $T(r)$ due to the Gaussian distribution of laser deposited energy (dotted baseline). The slower net radial crystallization through Zone III provides a better match with thermal diffusion and results in an approximately constant front temperature. The abrupt transition in crystallization dynamics occurs once $T(r)$ drops below a threshold for the radial ELPC process to occur.

abrupt change in the crystallization dynamics occurs once the temperature at the rapidly advancing Zone II crystallization front drops below the lower threshold for the ELPC process. This transition occurs after approximately 10 μm of Zone II growth in the geometry of our experiment.

The direct observation of the time-evolving microstructure presented here requires a revisiting of conclusions about this process that were drawn in the absence of such data. Earlier work has proposed that once Zone II crystallization is complete there is a pause in the crystallization as the heat initially deposited in the pump pulse traverses the LREC region[3] and that Zone III crystallization is initiated by the resulting rise in temperature.[3,10] In fact, it was suggested that Zone III crystallization proceeds at higher temperatures than Zone II due to this redistribution of thermal energy.[10] Such a view is inconsistent with the time-resolved measurements given here, since we do not observe such a delay in DTEM images of the time-evolving microstructure. Similarly, our data does not support an earlier model for Zone III crystallization suggesting that the observed layering forms through inward (i.e., radial) crystallization of thin bands of molten material.[10] Here we have clearly shown that, outside the transition region, the local growth front velocity is azimuthally directed in Zone III.

The dramatic change in crystallization behavior in Zone III produces patterns of crystallization orthogonal to the net radial heat flow and is accompanied by a reduction in the rate at which crystallization advances in the radial direction by almost an order of magnitude. Taken together with the thermal modeling results, the DTEM observations suggest another mechanism for Zone III crystallization and an explanation for the observed layered microstructure. Once $T(r)$ drops below T_{ma} the rapid ($\sim$10 m/s) radial advance of the Zone II dendrites by the ELPC mechanism can no longer be sustained; crystal growth has outpaced thermal diffusion and the crystallization front has penetrated into a region below the threshold temperature supporting this growth mode. Previous work has demonstrated the sensitive dependence of crystallization mode with substrate temperature in other geometries.[4,7] A similar mechanism can be supported, however, along the narrow ($\sim$1 μm) bands in the orthogonal direction where the crystallization front follows an approximately isothermal curve at the appropriate temperature. An important feature of this new growth mode is that it better matches the radial advance of crystallization with thermal diffusion in the radial direction (i.e., thermal diffusion of both the newly evolved energy at the crystallization front and that flowing from the previously crystallized Zone II). At ELPC growth rates a typical 8-μm long single layer is formed in $\sim$1 μs. The diffusion length over this period is $\sim$6 μm, sufficient to prepare a narrow adjacent band of material to support growth of an additional layer. The excellent match between thermal diffusion and the radial advance of crystallization is evident in the temperature profiles shown in Fig. 4, which show that this layered growth mode results in an almost constant temperature at the radius in which new layers are growing through Zone III. This growth mode is similar to the zigzag growth described by Chojnacka,[4] proposed for the observed scalloped microstructure in explosively crystallized films in a different experimental geometry.

The crystallization process in this zone ceases when the temperature of the adjacent amorphous material drops below a critical level and can no longer support growth of a new layer through the mechanism described above.

V. CONCLUSION

Recent enhancements in DTEM allow complex microstructural evolution to be followed with nanosecond temporal and nanometer spatial resolutions. Here we have applied this method to study nanosecond laser-driven crystallization of amorphous germanium films and DTEM has provided important insights into the crystallization dynamics and mechanisms involved in the formation of the three qualitatively distinct morphological zones evident in the final structure. Through direct measurements of the crystallization front, we have shown that growth through Zone II is subject to a Mullins-Sekerka-like instability that results in microscopically smooth dendrites that develop with increased faceting towards the boundary of this zone. We have also shown an abrupt transition in the nature of the crystal growth front in Zone III, where the growth of single-crystal regions is perpendicular to the macroscopic crystallization direction (or net heat flow), and that formation of the layered structure is consistent with a zigzag growth mode. The direct measurement of the time scales involved in the crystal growth and a comparison with thermal diffusion timescales show that crystallization in both Zones II and III is explosive in the sense that it is driven by latent heat released at the crystallization interface and not thermal diffusion of laser-deposited energy. These time scales suggest explosive liquid phase assisted phase transformation is the dominant mechanism in both Zone II and Zone III crystallization, despite the radial advance of crystallization preceding an order of magnitude more slowly in Zone III.

This study serves to emphasize the importance of time-resolved imaging for determining complex crystallization mechanisms, since under such circumstances the analysis of postmortem images is insufficient to uniquely determine the details of microstructural evolution. DTEM is now a mature approach for such studies and can/should be applied to a broad range of related problems in materials science where crystal nucleation and growth occur too rapidly to be studied with standard approaches, and the irreversible nature of the process precludes the use of related multishot time-resolved techniques.

ACKNOWLEDGMENTS

This work was funded in part by the Natural Science and Engineering Research Council of Canada (NSERC), Fonds de recherche du Québec-Nature et technologies and Ministère du Développement économique, Innovation et Exportation of Quebec. B.J.S. and F.R. acknowledge the support of the Canada Research Chairs program. L.N. acknowledges CGS Alexander Graham Bell and Michael Smith FSSA of NSERC. T.L., B.W.R., and G.H.C. were supported by the US Department of Energy, Office of Basic Energy Sciences, Division of Materials Sciences and Engineering. Work presented in this article was performed in part under the auspices of the US Department of Energy by Lawrence Livermore National Laboratory under Contract DE-AC52-07NA27344.

*To whom correspondence should be addressed: lagrange2@llnl.gov
†rosei@emt.inrs.ca
‡bradley.siwick@mcgill.ca

[1]G. Badertscher, R. Salathé, and H. Weber, Appl. Phys. A **25**, 91 (1981).
[2]O. Bostanjoglo, Phys. Status Solidi A **70**, 473 (1982).
[3]O. Bostanjoglo, R. P. Tornow, and W. Tornow, Ultramicroscopy **21**, 367 (1987).
[4]A. P. Chojnacka, Ph.D. thesis, Cornell University, 2002.
[5]A. G. Fitzgerald, J. Mater. Sci. Lett. **1**, 145 (1982).
[6]H. D. Geiler, E. Glaser, G. Gotz, and M. Wagner, J. App. Phys. **59**, 3091 (1986).
[7]C. Grigoropoulos, M. Rogers, S. H. Ko, A. A. Golovin, and B. J. Matkowsky, Phys. Rev. B **73**, 184125 (2006).
[8]H. J. Leamy, W. L. Brown, G. K. Celler, G. Foti, G. H. Gilmer, and J. C. C. Fan, Appl. Phys. Lett. **38**, 137 (1981).
[9]P. Pierrard, B. Mutaftschiev, W. Marine, J. Marfaing, and F. Salvan, Thin Solid Films **111**, 141 (1984).
[10]R. K. Sharma, S. K. Bansal, R. Nath, R. M. Mehra, K. Bahadur, R. P. Mall, K. L. Chaudhary, and C. L. Garg, J. Appl. Phys. **55**, 387 (1984).
[11]W. C. Sinke, A. Polman, S. Roorda, and P. A. Stolk, Appl. Surf. Sci. **43**, 128 (1989).
[12]T. Takamori, R. Messier, and R. Roy, J. Mater. Sci. **8**, 1809 (1973).
[13]T. Takamori, R. Messier, and R. Roy, J. Mater. Sci. **9**, 159 (1974).
[14]P. A. Stolk, A. Polman, and W. C. Sinke, Phys. Rev. B **47**, 5 (1993).
[15]M. O. Thompson, G. J. Galvin, J. W. Mayer, P. S. Peercy, J. M. Poate, D. C. Jacobson, A. G. Cullis, and N. G. Chew, Phys. Rev. Lett. **52**, 2360 (1984).
[16]E. J. Albenze, M. O. Thompson, and P. Clancy, Phys. Rev. B **70**, 094110 (2004).
[17]E. P. Donovan, F. Spaepen, D. Turnbull, J. M. Poate, and D. C. Jacobson, J. Appl. Phys. **57**, 1795 (1985).
[18]M. Posselt and A. Gabriel, Phys. Rev. B **80**, 045202 (2009).
[19]J. S. Kim, T. LaGrange, B. W. Reed, M. L. Taheri, M. R. Armstrong, W. E. King, N. D. Browning, and G. H. Campbell, Science **321**, 1472 (2008).
[20]T. LaGrange, G. H. Campbell, B. W. Reed, M. Taheri, J. B. Pesavento, J. S. Kim, and N. D. Browning, Ultramicroscopy **108**, 1441 (2008).
[21]B. W. Reed, M. R. Armstrong, N. D. Browning, G. H. Campbell, J. E. Evans, T. LaGrange, and D. J. Masiel, Microsc. Microanal. **15**, 272 (2009).
[22]B. W. Reed, T. LaGrange, R. M. Shuttlesworth, D. J. Gibson, G. H. Campbell, and N. D. Browning, Rev. Sci. Instrum. **81**, 053706 (2010).
[23]J. S. Kim, T. LaGrange, B. W. Reed, R. Knepper, T. P. Weihs, N. D. Browning, and G. H. Campbell, Acta Mater. **59**, 3571 (2011).
[24]T. LaGrange, G. H. Campbell, J. D. Colvin, B. Reed, and W. E. King, J. Mater. Sci. **41**, 4440 (2006).
[25]T. LaGrange, D. S. Grummon, B. W. Reed, N. D. Browning, W. E. King, and G. H. Campbell, Appl. Phys. Lett. **94**, 184101 (2009).
[26]H. S. Chen and D. Turnbull, J. Appl. Phys. **40**, 4214 (1969).
[27]R. Messier, T. Takamori, and R. Roy, Solid State Commun. **16**, 311 (1975).
[28]P. Nath and K. L. Chopra, Phys. Rev. B **10**, 3412 (1974).
[29]Z. Cao, P. Liu, X. Meng, S. Tang, and H. Lu, Appl. Phys. A **94**, 393 (2009).
[30]L. Nikolova, T. LaGrange, B. W. Reed, M. J. Stern, N. D. Browning, G. H. Campbell, J. C. Kieffer, B. J. Siwick, and F. Rosei, Appl. Phys. Lett. **97**, 203102 (2010).
[31]J. S. Langer, Rev. Mod. Phys. **52**, 1 (1980).
[32]W. W. Mullins and R. F. Sekerka, J. Appl. Phys. **34**, 323 (1963).
[33]D. A. Porter, K. E. Easterling, and M. Y. Sherif, *Phase Transformations in Metals and Alloys* (CRC Press, New York, 2009), p. 181.
[34]R. R. Hultgren, *Selected values of the thermodynamic properties of the elements* (American Society for Metals, Metals Park, Ohio, 1973).